photonics

MDPI

Article

Evolution of Specular and Antispecular Radially Polarized Partially Coherent Twisted Beams Blocked by an Opaque Obstacle

Miaomiao Tang *, Pengju Yuan, Yunzhe Yang, Yujie Zhou and Xinzhong Li

School of Physics and Engineering, Henan University of Science and Technology, Luoyang 471023, China
* Correspondence: tmiaomiao0371@163.com

Abstract

We introduce a class of specular and antispecular radially polarized partially coherent twisted beams by using a wavefront-folding interferometer and then investigate the propagation of such beams blocked by an opaque obstacle. One sees that these optical fields exhibit sharp internal spectral density with a central peak in the specular case and a central dip in the antispecular case. It is also seen that both the spectral density and the polarization feature present a good twist effect and a tendency to self-heal upon propagation. However, unlike the spectral density that can recover its profile perfectly, the self-healing ability of both the degree of polarization and the generalized Stokes parameters is only partial and not complete. While a smaller value of the twist factor enhances the self-healing performance of the beam field, it slows the beam's rotation and degrades the degree of polarization. Moreover, the polarization distribution in the central area is mainly determined by the phase difference of the interferometer. The results of our work have important applications in the fields of free-space beam communication and particle trapping.

Keywords: partially coherent beams; specular optical fields; propagation; statistical properties

1. Introduction

The self-healing property, which refers to the fact that the light beam can restore its initial profile over a certain distance after being partially blocked by an obstacle, was first found in Bessel beams [1–6]. Subsequently, such a phenomenon was found in other nondiffracting beams such as caustic beams [7] and Airy beams [8–10]. However, the self-healing ability is not exclusive to nondiffracting optical fields; some diffracting beams, including optical ring lattices [11], Pearcey beams [12], optical pillar arrays [13] and radially polarized Bessel beams [14], are also able to reconstitute their profile on propagation. It has been demonstrated that such a self-healing property offers significant applied value in micro-control, microscopy, and optical communications [15,16]. In recent decades, interest in partially coherent beams has been growing due to their unique features compared to fully coherent fields [17–19]. In 2016, Wang et al. successfully extended the self-healing concept to the partially coherent domain [20]. Zhou et al. demonstrated that the self-healing characteristic of partially coherent fields can be utilized in ghost imaging and coherent diffraction imaging [21]. Inspired by these works, the self-healing propagation of various partially coherent beams has been investigated [22–26]. Xu et al. studied the self-healing capacity of a Hermite–Gaussian correlated Schell-model beam and introduced a similarity degree to quantify the self-healing ability [23]. Peng et al. investigated the self-reconstruction of a twisted Laguerre–Gaussian Schell-model beam [24]. Liu et al.

Check for updates

Received: 11 March 2026
Revised: 8 April 2026
Accepted: 9 April 2026
Published: 11 April 2026

Copyright: © 2026 by the authors. Licensee MDPI, Basel, Switzerland. This article is an open access article distributed under the terms and conditions of the Creative Commons Attribution (CC BY) license.

investigated, both numerically and experimentally, the degree of coherence of a partially coherent vortex beam blocked by an opaque obstacle [25].

For convenience's sake, most partially coherent beams are described by the Schell mode, which implies that their spatial coherence only depends on the coordinate difference. However, this choice will inevitably overlook potential interesting features of random fields. An important exception is the specular partially coherent optical field [27,28], whose cross-spectral density satisfies the equation $W(-x_1, x_2) = W(x_1, -x_2)$. In 2015, specular partially coherent beams were demonstrated experimentally using a wavefront-folding interferometer (WFI), and the concept of an antispecular partially coherent field was introduced [29]. Since then, widespread attention has been aroused regarding specular (and antispecular) beam fields. Zhou et al. investigated the specularity of partially coherent beams propagating through atmospheric turbulence [30]. Guo et al. calculated the radiation forces on a Rayleigh dielectric particle produced by a specular optical field and then demonstrated that such a field presented substantial benefits for trapping high-index particles [31]. Das et al. produced specular and antispecular Bessel-correlated beams with a mirror-based WFI [32]. Tang et al. introduced a class of specular beams with non-trivial symmetries and various intensity profiles [33]. Moreover, the specular transformation has been extended to the electromagnetic domain, and it is demonstrated that the polarization properties of the specular fields are closely related to the initial state of polarization [34,35]. However, to the best of our knowledge, the disturbed propagation of specular beams has not been investigated.

Polarization is one of the most important properties of a light beam. In the past decade, studies of vector partially coherent beams with spatially nonuniform states of polarization were reported and interesting results were observed. In 2015, Wu introduced a radially polarized partially coherent twisted (RPPCT) beam and then investigated the propagation properties of the beam in free space [36]. Extensive research has been conducted on the propagation and scatting features of such a beam in uniaxial crystal, underwater turbulence medium and turbulent atmosphere [37–41]. These results show significant promise for the applications of the RPPCT beams in areas such as optical communication. In this work, we will firstly introduce the specular and antispecular RPPCT fields by inserting an RPPCT beam into a WFI and then investigate the propagation of the specular (or antispecular) field blocked by an opaque obstacle. The self-healing property of the spectral density, the degree of polarization (DOP), and the generalized Stokes parameters are illustrated by numerical examples. The impacts of the twist factor, the source coherence, and the WFI on the beam features are demonstrated.

2. Theoretical Models of Specular and Antispecular RPPCT Beams

Let us assume that a partially coherent electromagnetic beam is incident on the WFI. The setup of the WFI is depicted schematically in Figure 1. The statistical features of the input plane ($z' = 0$) could be characterized by the 2×2 cross-spectral density matrix (CSDM) as follows [42]:

$$\mathbf{W}_0(\boldsymbol{\rho}_1', \boldsymbol{\rho}_2') = \left\langle \mathbf{E}_0^*(\boldsymbol{\rho}_1') \mathbf{E}_0^T(\boldsymbol{\rho}_2') \right\rangle = \begin{bmatrix} W_{0xx}(\boldsymbol{\rho}_1', \boldsymbol{\rho}_2') & W_{0xy}(\boldsymbol{\rho}_1', \boldsymbol{\rho}_2') \\ W_{0yx}(\boldsymbol{\rho}_1', \boldsymbol{\rho}_2') & W_{0yy}(\boldsymbol{\rho}_1', \boldsymbol{\rho}_2') \end{bmatrix}, \tag{1}$$

where $\boldsymbol{\rho}_1' = (x_1', y_1')$ and $\boldsymbol{\rho}_2' = (x_2', y_2')$ are two position vectors in the source plane. The asterisk and the superscript T denote the conjugated and transposed complex, respectively. The CSDM elements in the output plane of the WFI, arising from the specular transformation, are described as [35]

$$\begin{aligned} W_{\alpha\beta}(\boldsymbol{\rho}_1', \boldsymbol{\rho}_2') &= \tfrac{L_{\alpha\beta}}{2}\left[W_{0\alpha\beta}(x_1', -y_1', x_2', -y_2') + W_{0\alpha\beta}(-x_1', y_1', -x_2', y_2')\right] \\ &+ \tfrac{L_{\alpha\beta}}{2}\left[W_{0\alpha\beta}(x_1', -y_1', -x_2', y_2')\exp(i\phi) + W_{0\alpha\beta}(-x_1', y_1', x_2', -y_2')\exp(-i\phi)\right], \end{aligned} \tag{2}$$

with $\alpha, \beta \in (x, y)$ and ϕ being the phase delay between the two arms of the WFI. Here $L_{\alpha\beta} = 1$ when $\alpha = \beta$ and $L_{\alpha\beta} = -1$ when $\alpha \neq \beta$. Thus, the output field satisfies the condition $\mathbf{W}(-\boldsymbol{\rho}_1', \boldsymbol{\rho}_2') = \mathbf{W}(\boldsymbol{\rho}_1', \boldsymbol{\rho}_2')$ if $\phi = 2\pi q$, and thereby the output field is specular. If $\phi = \pi + 2\pi q$, we have $\mathbf{W}(-\boldsymbol{\rho}_1', \boldsymbol{\rho}_2') = -\mathbf{W}(\boldsymbol{\rho}_1', \boldsymbol{\rho}_2')$ and, thus, the output field is antispecular.

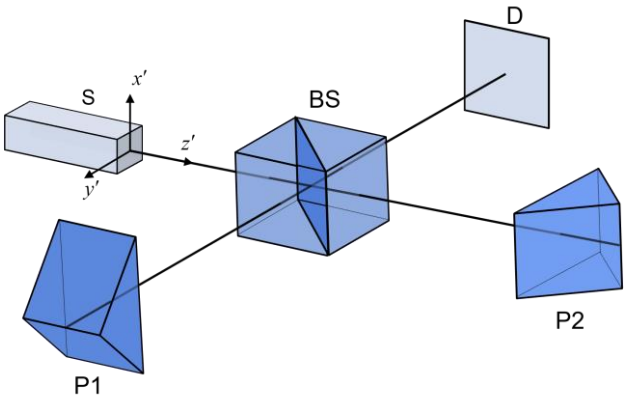


Figure 1. Configuration schematic of the WFI: S is the source, BS is a non-polarizing beam splitter, P1 and P2 are right-angle prisms, and D is a detector. The operation of this device is based on two right-angle prisms, P1 and P2, placed vertically, where P1 reflects the incident beam field in the x' direction and P2 reflects the incident beam field in the y' direction.

We consider an RPPCT beam incident on the WFI. The CSDM elements of the source take the following form [36]

$$\begin{aligned} W_{0\alpha\beta}(\boldsymbol{\rho}_1', \boldsymbol{\rho}_2') &= \tfrac{\alpha_1\beta_2}{w_0^2}\exp\left(-\tfrac{x_1'^2 + x_2'^2 + y_1'^2 + y_2'^2}{4w_0^2}\right) \\ &\times \exp\left[-\tfrac{(x_1' - x_2')^2 + (y_1' - y_2')^2}{2\delta_0^2}\right]\exp\left[-iku(x_1'y_2' - x_2'y_1')\right], \end{aligned} \tag{3}$$

where $k = 2\pi/\lambda$ is the wavenumber with λ being the wavelength. w_0 and δ_0 denote the beam width and the source coherence length, respectively. u is the twist factor, which must satisfy the condition $|u| \leq 1/k\delta_0^2$.

By substituting Equation (3) into Equation (2), one obtains the CSDM elements of the output field as

$$\begin{aligned} W_{\alpha\beta}(\boldsymbol{\rho}_1', \boldsymbol{\rho}_2') &= \tfrac{\alpha_1\beta_2}{w_0^2}\exp\left(-\tfrac{x_1'^2 + x_2'^2 + y_1'^2 + y_2'^2}{4w_0^2}\right)\left\{\exp\left[-\tfrac{(x_1' - x_2')^2 + (y_1' - y_2')^2}{2\delta_0^2}\right]\right. \\ &\times \exp\left[iku(x_1'y_2' - x_2'y_1')\right] - \exp\left[-\tfrac{(x_1' + x_2')^2 + (y_1' + y_2')^2}{2\delta_0^2}\right] \\ &\left.\times \exp\left[iku(x_2'y_1' - x_1'y_2')\cos\phi\right]\right\}, \end{aligned} \tag{4}$$

As can be seen, we have a specular (antispecular) RPPCT beam if $\phi = 2\pi q (\phi = \pi + 2\pi q)$.

Specular and antispecular RPPCT beams could be experimentally generated using a method akin to that described in [29,43]. First, the CSDM of the RPPCT beam in Equation (3) is formed by using a spatial light modulation and the polarization modulation technique. Then, the specular transformation is executed using a WFI. Another WFI, with non-imaging polarization elements, is used to characterize the properties of the output field.

3. Propagation of the Beam Field Obstructed by an Opaque Obstacle

Consider the WFI output field as a second source ($z = 0$), which is partially blocked by an opaque obstacle in the WFI output and propagates toward a receiver plane (see Figure 2). To simplify the calculation, we assume that the obstacle is circular and has a Gaussian absorption efficiency. Therefore, the transmission function $T(\boldsymbol{\rho}_i')$ of the opaque obstacle can be expressed as [22]:

$$T(\boldsymbol{\rho}_i') = 1 - \exp\left(-\frac{\boldsymbol{\rho}_i' - \boldsymbol{\rho}_0'}{w_d^2}\right), \tag{5}$$

with $\boldsymbol{\rho}_0 = (x_0, y_0)$ denoting the vector point position of the opaque obstacle and w_d representing the size of the obstacle.

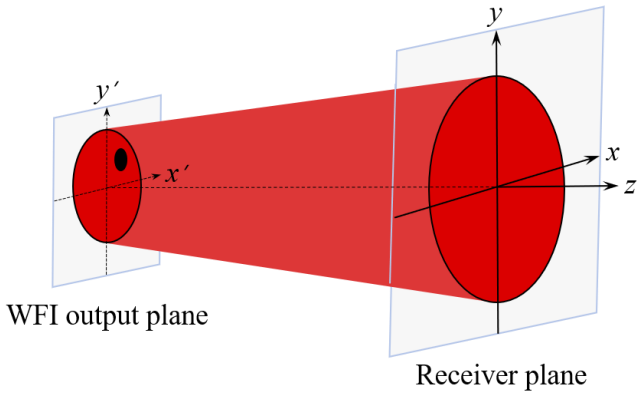


Figure 2. Schematic representation of optical geometry.

The field at any distance z from the WFI output could be obtained by using the generalized Huygens–Fresnel formula

$$\begin{aligned} W_{\alpha\beta}(\boldsymbol{\rho}_1, \boldsymbol{\rho}_2, z) &= \left(\frac{k}{2\pi z}\right)^2 \iint\iint \mathrm{d}^2\boldsymbol{\rho}_1' \mathrm{d}^2\boldsymbol{\rho}_2' T^*(\boldsymbol{\rho}_1') T(\boldsymbol{\rho}_2')_2 W_{\alpha\beta}(\boldsymbol{\rho}_1', \boldsymbol{\rho}_2') \\ &\times \exp\left[-ik\frac{(\boldsymbol{\rho}_1 - \boldsymbol{\rho}_1')^2 - (\boldsymbol{\rho}_2 - \boldsymbol{\rho}_2')^2}{2z}\right], \end{aligned} \tag{6}$$

where $\boldsymbol{\rho}_1 = (x_1, y_1)$ and $\boldsymbol{\rho}_2 = (x_2, y_2)$ represent the position vectors in the receiver plane.

By substituting Equation (6) into Equation (5), one obtains

$$\begin{aligned} W_{\alpha\beta}(\boldsymbol{\rho}_1, \boldsymbol{\rho}_2, z) &= \left(\frac{k}{2\pi z}\right)^2 \iint\iint \mathrm{d}^2\boldsymbol{\rho}_1' \mathrm{d}^2\boldsymbol{\rho}_2' \left[1 - \exp\left(-\frac{\boldsymbol{\rho}_1' - \boldsymbol{\rho}_0'}{w_d^2}\right) - \exp\left(-\frac{\boldsymbol{\rho}_2' - \boldsymbol{\rho}_0'}{w_d^2}\right)\right. \\ &\left. + \exp\left(-\frac{\boldsymbol{\rho}_1' - \boldsymbol{\rho}_0'}{w_d^2}\right) \exp\left(-\frac{\boldsymbol{\rho}_2' - \boldsymbol{\rho}_0'}{w_d^2}\right)\right] W_{\alpha\beta}(\boldsymbol{\rho}_1', \boldsymbol{\rho}_2') \\ &\times \exp\left[-ik\frac{(\boldsymbol{\rho}_1 - \boldsymbol{\rho}_1')^2 - (\boldsymbol{\rho}_2 - \boldsymbol{\rho}_2')^2}{2z}\right]. \end{aligned} \tag{7}$$

By substituting Equation (4) into Equation (7), the CSDM elements on propagation could be rewritten as

$$W_{\alpha\beta}(\boldsymbol{\rho}_1, \boldsymbol{\rho}_2, z) = W1_{\alpha\beta}(\boldsymbol{\rho}_1, \boldsymbol{\rho}_2, z) - W2_{\alpha\beta}(\boldsymbol{\rho}_1, \boldsymbol{\rho}_2, z) - W3_{\alpha\beta}(\boldsymbol{\rho}_1, \boldsymbol{\rho}_2, z) + W4_{\alpha\beta}(\boldsymbol{\rho}_1, \boldsymbol{\rho}_2, z), \tag{8}$$

with

$$
\begin{aligned}
W1_{\alpha\beta}(\boldsymbol{\rho}_1,\boldsymbol{\rho}_2,z) &= \left(\frac{k}{2\pi z}\right)^2 \iint\iint \mathrm{d}^2\boldsymbol{\rho}_1'\mathrm{d}^2\boldsymbol{\rho}_2' \frac{\alpha_1\beta_2}{w_0^2}\exp\left(-\frac{x_1'^2+x_2'^2+y_1'^2+y_2'^2}{4w_0^2}\right)\\
&\times\exp\left[-ik\frac{(\boldsymbol{\rho}_1-\boldsymbol{\rho}_1')^2-(\boldsymbol{\rho}_2-\boldsymbol{\rho}_2')^2}{2z}\right]\left\{\exp\left[-\frac{(x_1'-x_2')^2+(y_1'-y_2')^2}{2\delta_0^2}\right]\right.\\
&\times\exp\left[iku(x_1'y_2'-x_2'y_1')\right]-\exp\left[-\frac{(x_1'+x_2')^2+(y_1'+y_2')^2}{2\delta_0^2}\right]\\
&\left.\times\exp\left[iku(x_2'y_1'-x_1'y_2')\cos\phi\right]\right\},
\end{aligned}
\tag{9}
$$

$$
\begin{aligned}
W2_{\alpha\beta}(\boldsymbol{\rho}_1,\boldsymbol{\rho}_2,z) &= \left(\frac{k}{2\pi z}\right)^2 \iint\iint \mathrm{d}^2\boldsymbol{\rho}_1'\mathrm{d}^2\boldsymbol{\rho}_2' \frac{\alpha_1\beta_2}{w_0^2}\exp\left(-\frac{\boldsymbol{\rho}_1'-\boldsymbol{\rho}_0'}{w_d^2}\right)\exp\left(-\frac{x_1'^2+x_2'^2+y_1'^2+y_2'^2}{4w_0^2}\right)\\
&\times\exp\left[-ik\frac{(\boldsymbol{\rho}_1-\boldsymbol{\rho}_1')^2-(\boldsymbol{\rho}_2-\boldsymbol{\rho}_2')^2}{2z}\right]\left\{\exp\left[-\frac{(x_1'-x_2')^2+(y_1'-y_2')^2}{2\delta_0^2}\right]\right.\\
&\times\exp\left[iku(x_1'y_2'-x_2'y_1')\right]-\exp\left[-\frac{(x_1'+x_2')^2+(y_1'+y_2')^2}{2\delta_0^2}\right]\\
&\left.\times\exp\left[iku(x_2'y_1'-x_1'y_2')\cos\phi\right]\right\},
\end{aligned}
\tag{10}
$$

$$
\begin{aligned}
W3_{\alpha\beta}(\boldsymbol{\rho}_1,\boldsymbol{\rho}_2,z) &= \left(\frac{k}{2\pi z}\right)^2 \iint\iint \mathrm{d}^2\boldsymbol{\rho}_1'\mathrm{d}^2\boldsymbol{\rho}_2' \frac{\alpha_1\beta_2}{w_0^2}\exp\left(-\frac{\boldsymbol{\rho}_2'-\boldsymbol{\rho}_0'}{w_d^2}\right)\exp\left(-\frac{x_1'^2+x_2'^2+y_1'^2+y_2'^2}{4w_0^2}\right)\\
&\times\exp\left[-ik\frac{(\boldsymbol{\rho}_1-\boldsymbol{\rho}_1')^2-(\boldsymbol{\rho}_2-\boldsymbol{\rho}_2')^2}{2z}\right]\left\{\exp\left[-\frac{(x_1'-x_2')^2+(y_1'-y_2')^2}{2\delta_0^2}\right]\right.\\
&\times\exp\left[iku(x_1'y_2'-x_2'y_1')\right]-\exp\left[-\frac{(x_1'+x_2')^2+(y_1'+y_2')^2}{2\delta_0^2}\right]\\
&\left.\times\exp\left[iku(x_2'y_1'-x_1'y_2')\cos\phi\right]\right\},
\end{aligned}
\tag{11}
$$

and

$$
\begin{aligned}
W4_{\alpha\beta}(\boldsymbol{\rho}_1,\boldsymbol{\rho}_2,z) &= \left(\frac{k}{2\pi z}\right)^2 \iint\iint \mathrm{d}^2\boldsymbol{\rho}_1'\mathrm{d}^2\boldsymbol{\rho}_2' \frac{\alpha_1\beta_2}{w_0^2}\exp\left(-\frac{\boldsymbol{\rho}_1'-\boldsymbol{\rho}_0'}{w_d^2}\right)\exp\left(-\frac{\boldsymbol{\rho}_2'-\boldsymbol{\rho}_0'}{w_d^2}\right)\\
&\times\exp\left(-\frac{x_1'^2+x_2'^2+y_1'^2+y_2'^2}{4w_0^2}\right)\exp\left[-ik\frac{(\boldsymbol{\rho}_1-\boldsymbol{\rho}_1')^2-(\boldsymbol{\rho}_2-\boldsymbol{\rho}_2')^2}{2z}\right]\\
&\times\left\{\exp\left[-\frac{(x_1'-x_2')^2+(y_1'-y_2')^2}{2\delta_0^2}\right]\exp\left[iku(x_1'y_2'-x_2'y_1')\right]\right.\\
&\left.-\exp\left[-\frac{(x_1'+x_2')^2+(y_1'+y_2')^2}{2\delta_0^2}\right]\exp\left[iku(x_2'y_1'-x_1'y_2')\cos\phi\right]\right\}.
\end{aligned}
\tag{12}
$$

Recalling these formula

$$\int_{-\infty}^{+\infty}\exp\left(-px^2\pm qx\right)dx=\sqrt{\frac{\pi}{p}}\exp\left(\frac{q^2}{4p^2}\right), \tag{13}$$

$$\int_{-\infty}^{+\infty}x\exp\left(-px^2\pm qx\right)dx=\frac{q}{2p}\sqrt{\frac{\pi}{p}}\exp\left(\frac{q^2}{4p^2}\right), \tag{14}$$

$$\int_{-\infty}^{+\infty}x^2\exp\left(-px^2\pm qx\right)dx=\frac{1}{2p}\left(1+\frac{q^2}{2p}\right)\sqrt{\frac{\pi}{p}}\exp\left(\frac{q^2}{4p^2}\right). \tag{15}$$

Then, after tedious but straightforward calculations, the analytical expression of the CSDM elements in any receiver plane could be obtained. The propagation features of the field could be analyzed by these expressions.

The spectral density and the DOP could be obtained as [42]

$$S(\boldsymbol{\rho},z)=\mathrm{Tr}[\mathbf{W}(\boldsymbol{\rho},\boldsymbol{\rho},z)], \tag{16}$$

and

$$P(\boldsymbol{\rho}, z) = \sqrt{1 - \frac{4\mathrm{Det}[\mathbf{W}(\boldsymbol{\rho}, \boldsymbol{\rho}, z)]}{\mathrm{Tr}[\mathbf{W}(\boldsymbol{\rho}, \boldsymbol{\rho}, z)]}}, \tag{17}$$

where Det and Tr stand for determinant and trace of the matrix, respectively.

The state of polarization could be examined by the generalized Stokes parameters, which are defined as [44]

$$S_0(\boldsymbol{\rho}, z) = W_{xx}(\boldsymbol{\rho}, \boldsymbol{\rho}, z) + W_{yy}(\boldsymbol{\rho}, \boldsymbol{\rho}, z), \tag{18}$$

$$S_1(\boldsymbol{\rho}, z) = W_{xx}(\boldsymbol{\rho}, \boldsymbol{\rho}, z) - W_{yy}(\boldsymbol{\rho}, \boldsymbol{\rho}, z), \tag{19}$$

$$S_2(\boldsymbol{\rho}, z) = W_{xy}(\boldsymbol{\rho}, \boldsymbol{\rho}, z) - W_{yx}(\boldsymbol{\rho}, \boldsymbol{\rho}, z), \tag{20}$$

$$S_3(\boldsymbol{\rho}, z) = i\big[W_{yx}(\boldsymbol{\rho}, \boldsymbol{\rho}, z) - W_{xy}(\boldsymbol{\rho}, \boldsymbol{\rho}, z)\big]. \tag{21}$$

The Stokes parameters have the following interpretations: $S_0(\boldsymbol{\rho}, z)$ represents the spectral density, while $S_1(\boldsymbol{\rho}, z)$, $S_2(\boldsymbol{\rho}, z)$, and $S_3(\boldsymbol{\rho}, z)$ are the difference between x and y polarized, $+\pi/4$ and $-\pi/4$ linearly polarized, and right-hand and left-hand circularly polarized average spectral density, respectively.

4. Results and Discussion

Now, we present the numerical analysis of the typical properties, including the spectral density, the DOP, and the normalized Stokes parameters of the specular and antispecular RPPCT beams obstructed by an opaque obstacle. In the following examples, the center of the obstacle is set at the position $\boldsymbol{\rho}_0 = (0.75\ \mathrm{mm}, 0.75\ \mathrm{mm})$ and the size of the obstacle is set as $w_d = 0.3$ mm. The wavelength is given as 632.8 mm and the beam width is set to be $w_0 = 1.5$ mm. Unless specified in captions, the other parameters are chosen as: $\delta_0 = 0.1$ mm and $u = 0.0006\ \mathrm{mm}^{-1}$, which satisfies the inequality $|u| \leq 1/k\delta_0^2$.

Figure 3 displays the normalized spectral density of the field at selected propagation distances. Row 1 and row 3 illustrate the beam profiles for the specular ($\phi = 0$) and antispecular ($\phi = \pi$) beam fields, whereas row 2 shows the normalized spectral density in the case $\phi = \pi/2$. A comparison of images in the first column reveals that the spectral density in the source plane remains unaffected by the phase difference of the WFI, and all images show identical profiles with a blocking effect. When increasing the propagation distance, the initial defect arising from the obstacle gradually diminishes and eventually disappears. Figure 3 further indicates that the spectral density in the beam center is mainly controlled by the WFI. The beam field owns a sharp central peak in the specular case during propagation, whereas it has a dark central dip in the antispecular case. Additionally, the self-healing speed of the beam profile is independent of the phase delay. Figure 4 illustrates the influence of the coherence width of the source on the far-field spectral density, for both specular and antispecular fields. It is seen that the area of the sharp central profile is determined by the value of the coherence width. A reduction in the coherence width leads to an expansion of the central peak (or dip).

Figure 5 shows the normalized spectral density of the antispecular field on propagation with selected twist factors. One finds that the twist factor not only governs the rotation of the beam spot but also determines the self-healing property of the field. A larger twisted factor will enhance the rotational effect; however, it degrades the self-healing performance, even preventing recovery in the far zone, as seen in Figure 5(b4,c4). In contrast, a smaller twist factor slows the rotation of the field while accelerating the recovery of the spectral density.

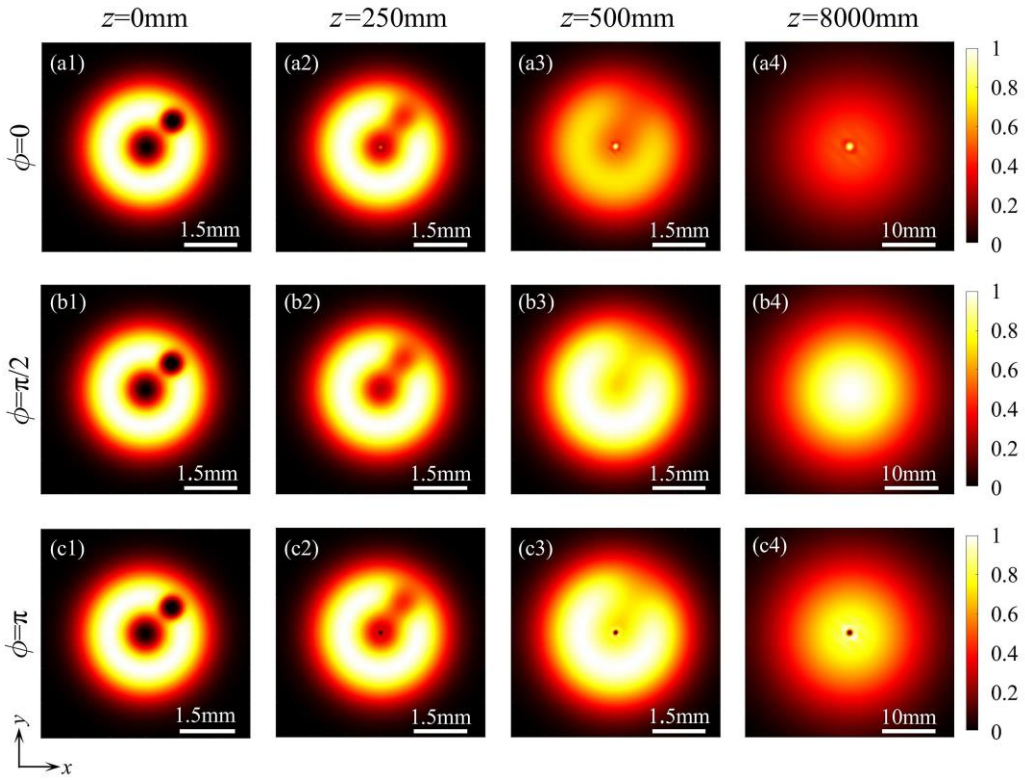


Figure 3. Normalized spectral density of specular (**a1**–**a4**), non-specular (**b1**–**b4**), and antispecular (**c1**–**c4**) beams at different propagation distances.

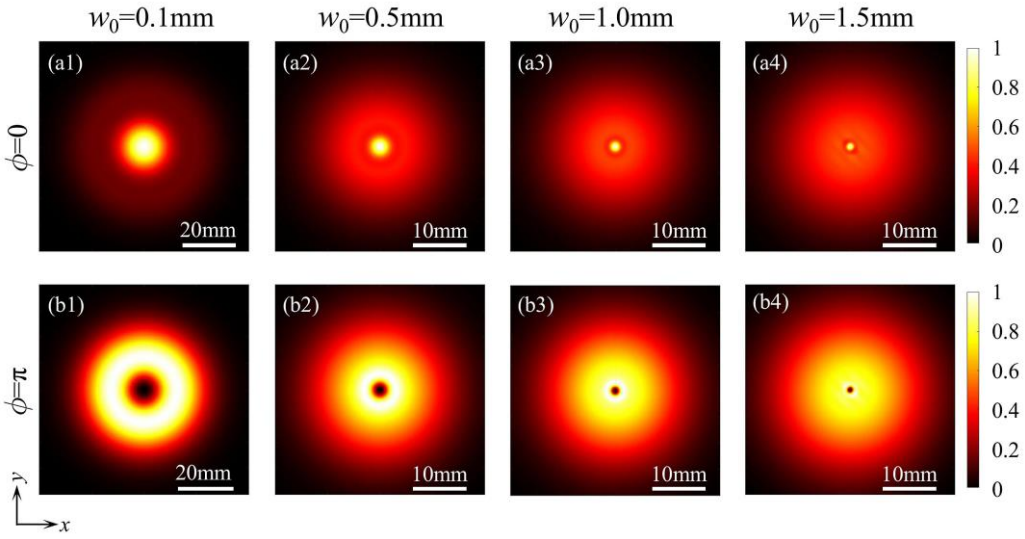


Figure 4. Normalized spectral density of specular (**a1**–**a4**) and antispecular (**b1**–**b4**) beams at the propagation distance $z = 8000$ mm with different coherence widths.

Now let us pay attention to the polarization properties of the field. Figure 6 shows the evolution of the degree of polarization of the specular and antispecular field, in row 1 and row 3, respectively. The corresponding situation for the case $\phi = \pi/2$ is shown in row 2. It is noted from the first column that the source plane is fully polarized $(P = 1)$ without obstacle-induced disturbance, which is completely different from the case of spectral density. As the propagation distance increases, the beam field undergoes depolarization, resulting in a partially polarized field. The presence of the obstacle caused the polarization to exhibit an asymmetric distribution, and a decrease in the degree of polarization is observed in the region influenced by the obstacle. The polarization rotates counterclockwise by 90 degrees

as the beam propagates and exhibits a certain degree of self-healing capability. However, unlike the spectral density, it is only partial and not complete. We also observe that the degree of polarization in the center is totally controlled by the WFI.

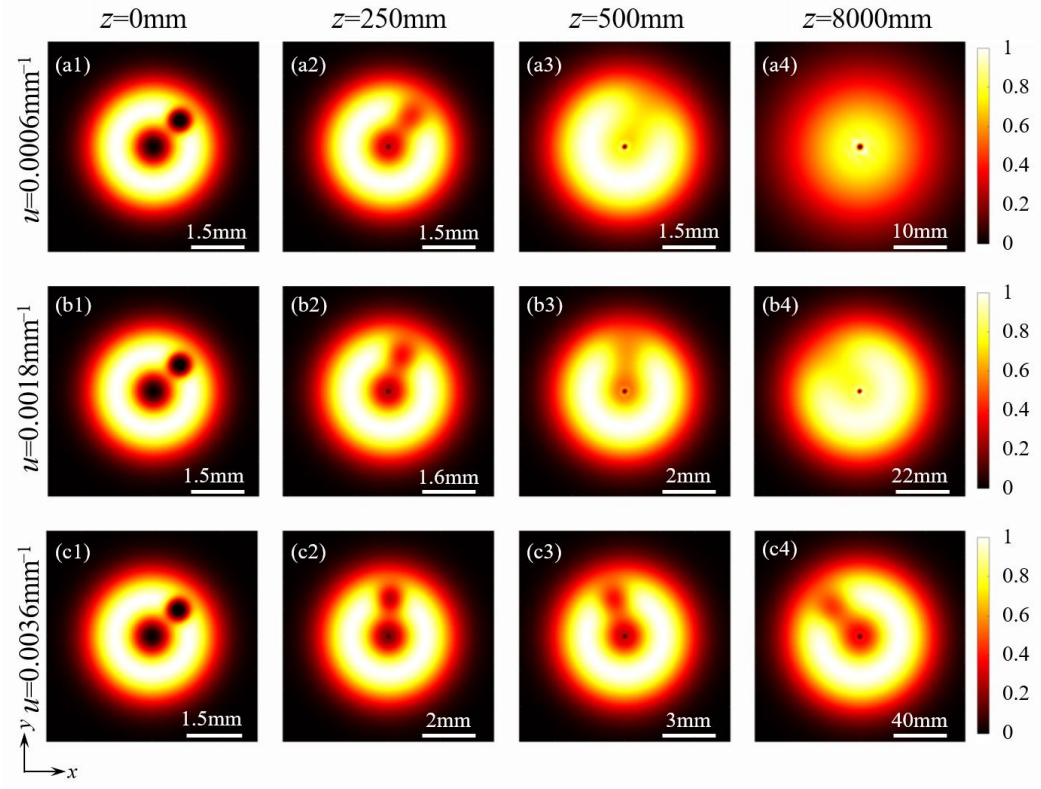


Figure 5. Normalized spectral density of the antispecular beam at different propagation distances with selected twisted factors. (**a1–a4**) $u = 0.0006$ mm^{-1}; (**b1–b4**) $u = 0.0018$ mm^{-1}; (**c1–c4**) $u = 0.0036$ mm^{-1}.

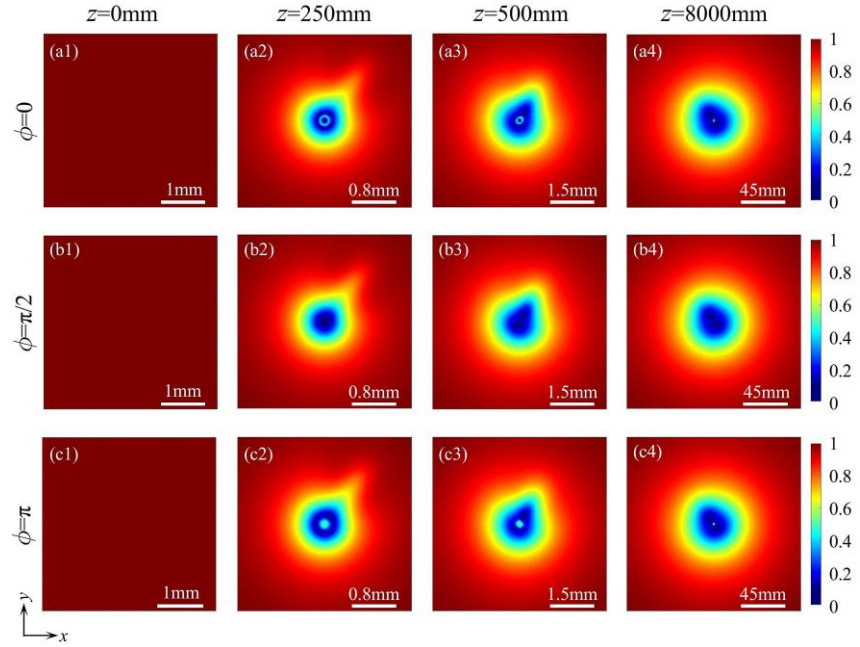


Figure 6. DOP of specular (**a1–a4**), non-specular (**b1–b4**), and antispecular (**c1–c4**) beams at different propagation distances.

Figure 7 shows the influence of the twist factor and the source coherence on the DOP of the specular field. One sees that reducing the twist strength enhances the self-healing ability

of the DOP; however, it also accelerates the decline of the polarization. Moreover, a larger value of coherence width leads to a lower degradation in polarization. Figure 8 displays the DOP in the central area with various phase delays and twisted factors. Compared to the RPPCT beam field ($\phi = \pi/2$), the transformed RPPCT fields preserve an oscillating DOP distribution in the beam center. As the twist factor decreases, the oscillations on the DOP become more evident. It is revealed that the transformed fields with different phase delays share an identical DOP at the on-axis points, which grows with the increase of the twisted factor. It is also interesting to note that in the presence of the obstacle the symmetric DOP distribution is destroyed to some extent.

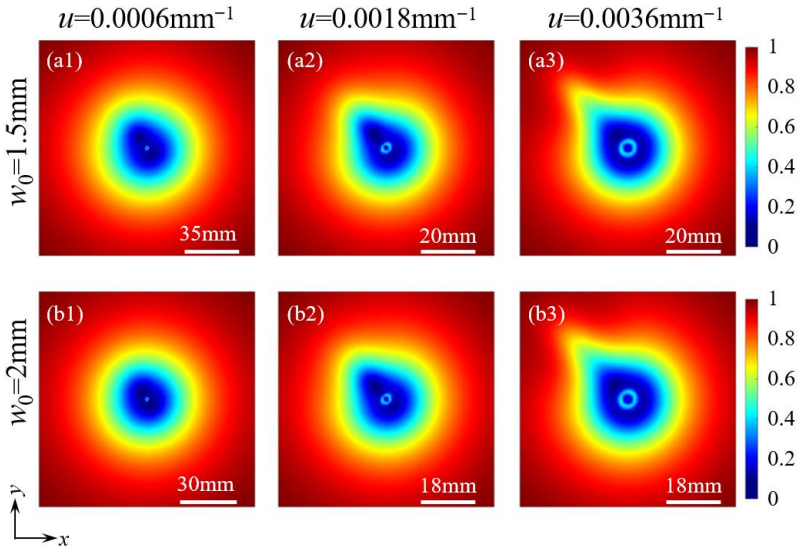


Figure 7. DOP of the specular beam at the propagation distance $z = 8000$ mm with different coherence widths and twist factors. (**a1–a3**) $w_0 = 1.5$ mm; (**b1–b3**) $w_0 = 2$ mm.

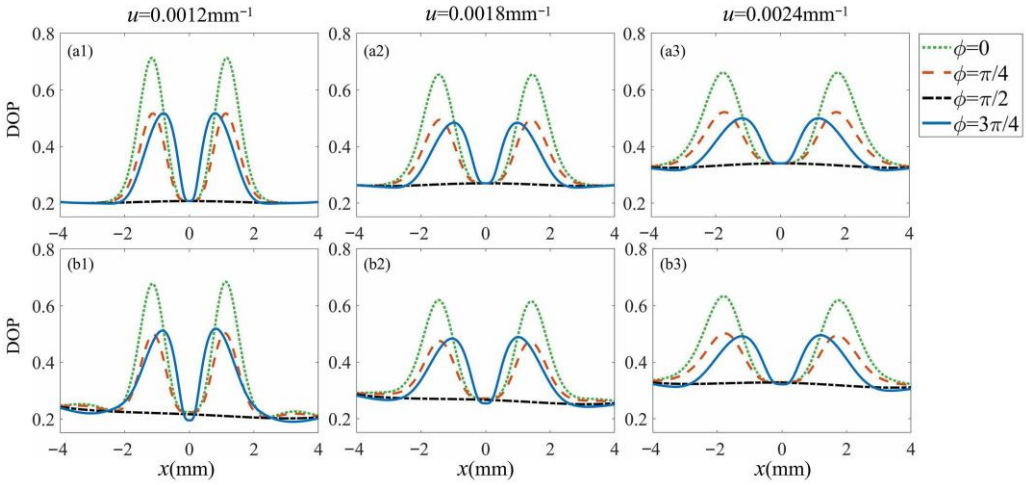


Figure 8. DOP of the transformed field along the x axis at the propagation distance $z = 8000$ mm with different twist factors. (**a1–a3**) the case without the obstacle; (**b1–b3**) the case with the obstacle.

The evolution of the normalized Stokes parameters S_1/S_0, S_2/S_0 and S_3/S_0 for both specular and antispecular fields is shown in Figures 9 and 10, respectively. One clearly sees that all parameters in the source plane are not influenced by the obstacle and the WFI. As the beam propagates, the disturbance from the obstacle becomes evident on the normalized Stokes parameters. Compared to S_3/S_0, S_1/S_0 and S_2/S_0 demonstrate superior resistance to the obstacle. This implies that circularly polarized light is much less restored than

linearly polarized light. S_1/S_0 and S_2/S_0 restore a symmetric distribution in the far field, whereas the profile for S_3/S_0 remains perturbed. Due to the existence of the twist phase of the source, all Stokes parameters rotate 90 degrees counterclockwise upon propagation, just as observed of the spectral density and the DOP. By comparing Figures 9 and 10, one finds that while S_3/S_0 shows the same evolution behavior in both specular and antispecular cases, the other Stokes parameters exhibit different central patterns in the two cases.

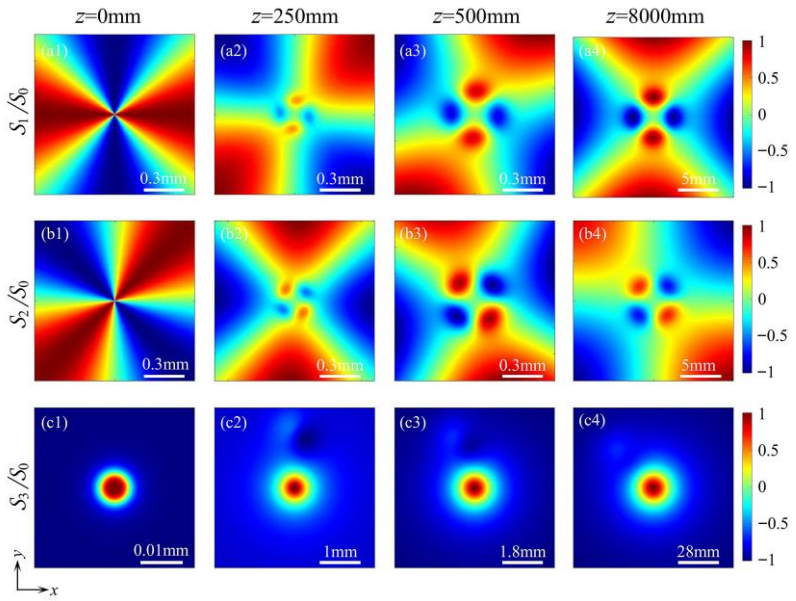


Figure 9. Generalized Stokes parameters of the specular RPPCT beam at different propagation distances. (**a1–a4**) S_1/S_0; (**b1–b4**) S_2/S_0; (**c1–c4**) S_3/S_0.

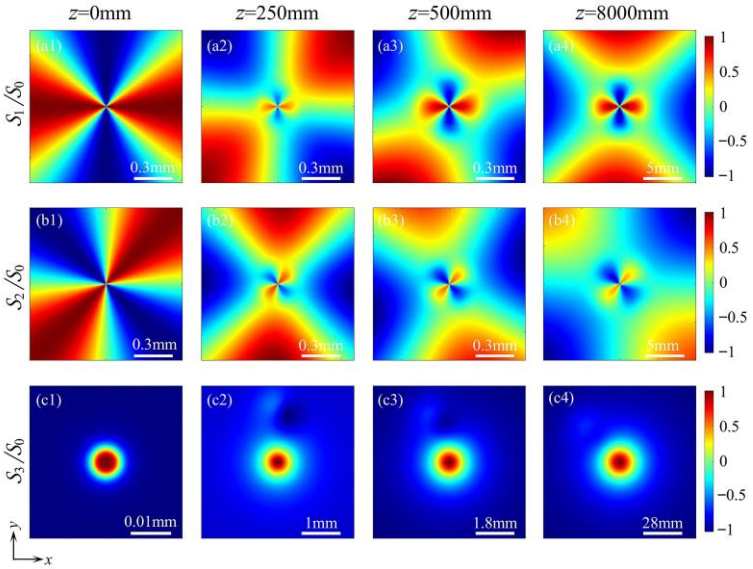


Figure 10. Generalized Stokes parameters of the antispecular RPPCT beam at different propagation distances. (**a1–a4**) S_1/S_0; (**b1–b4**) S_2/S_0; (**c1–c4**) S_3/S_0.

In previous studies, the self-healing properties of partially coherent fields mainly focused on the Schell-model beams, such as the Gaussian Schell-model beams [22], the Hermite–Gaussian correlated Schell-model beams [23], and the Laguerre–Gaussian Schell-model beams [24]. It is well known that the Schell model is the most commonly used model, in which the degree of spatial coherence only depends on coordinated difference. However, this model will inevitably overlook potential interesting features of random fields.

In our study, we introduce a class of specular and antispecular RPPCT fields which possess non-Schell correlations and then investigate the evolution of the specular (or antispecular) field blocked by an opaque obstacle. The most interesting finding is that these fields exhibit sharp internal spectral density with a central peak in the specular case and a central dip in the antispecular case. The polarization properties in the central area of the beam could be flexibly controlled by adjusting the phase delay of the WFI. This characteristic is entirely distinct from beam fields with the Schell model. Moreover, both the spectral density and the polarization feature present a good twist effect and a tendency to self-heal upon propagation. These results are of particular importance in free-space communications and ghost imaging.

5. Conclusions

We presented a class of specular and antispecular RPPCT light beams by inserting an RPPCT beam into a WFI and then studied the disturbed propagation of such fields. The evolution behavior of the spectral density, the DOP, and the generalized Stokes parameters are illustrated by numerical examples. We demonstrate that these fields exhibit sharp internal spectral density with a central peak in the specular case and a central dip in the antispecular case. It is also found that the twist strength not only controls the rotation of the spectral density but also modulates its self-healing property. While a larger value of the twist factor enhances the beam's rotation, it degrades the self-healing performance. To some extent, the spot profile may fail to recover perfectly with an excessive twist factor. Compared with the spectral density, the self-healing ability of both the DOP and the generalized Stokes parameters is only partial and not complete. Reducing the twist strength could improve the self-healing ability of the polarization, at the expense of accelerating the decline of the DOP. Moreover, the polarization distribution in the central area of the beam is determined by the phase delay of the WFI and the coherence of the source.

Author Contributions: Conceptualization, M.T.; Data curation, P.Y. and Y.Z.; Methodology, Y.Y.; Project administration, M.T. and X.L.; Software, P.Y. and Y.Y.; Supervision, X.L.; Writing—original draft, M.T. and P.Y.; Writing—review and editing, M.T. and X.L. All authors have read and agreed to the published version of the manuscript.

Funding: This research was funded by the National Natural Science Foundation of China (No. 12174089, 12504345) and the Natural Science Foundation of Henan Province (No. 222300420042).

Data Availability Statement: Data is contained within the article.

Conflicts of Interest: The authors declare no conflicts of interest.

References

1. Durnin, J.; Miceli, J.J.; Eberly, J.H. Diffraction-free beams. *Phys. Rev. Lett.* **1987**, *58*, 1499–1501. [CrossRef] [PubMed]
2. Durnin, J. Exact solutions for nondiffracting beams. I. The scalar theory. *J. Opt. Soc. Am. A* **1987**, *4*, 651–654. [CrossRef]
3. Sogomonian, S.; Klewitz, S.; Herminghaus, S. Self-reconstruction of a Bessel beam in a nonlinear medium. *Opt. Commun.* **1997**, *139*, 313–319. [CrossRef]
4. Bouchal, Z.; Wagner, J.; Chlup, M. Self-reconstruction of a distorted nondiffracting beam. *Opt. Commun.* **1998**, *151*, 207–211. [CrossRef]
5. Tao, S.H.; Yuan, X. Self-reconstruction property of fractional Bessel beams. *J. Opt. Soc. Am. A* **2004**, *21*, 1192–1197. [CrossRef] [PubMed]
6. Chu, X. Analytical study on the self-healing property of Bessel beam. *Eur. Phys. J. D* **2012**, *66*, 259. [CrossRef]
7. Anguiano-Morales, M.; Martínez, A.; Iturbe-Castillo, M.D.; Chávez-Cerda, S.; Alcalá-Ochoa, N. Self-healing property of a caustic optical beam. *Appl. Opt.* **2007**, *46*, 8284–8290. [CrossRef]
8. Broky, J.; Siviloglou, G.; Dogariu, A.; Christodoulides, D. Self-healing properties of optical Airy beams. *Opt. Express* **2008**, *16*, 12880–12891. [CrossRef] [PubMed]
9. Chu, X.; Zhou, G.; Chen, R. Analytical study of the self-healing properties of Airy beams. *Phys. Rev. A* **2012**, *85*, 013815. [CrossRef]

10. Chu, X.; Li, X.; Chen, L. Evolution of an Airy beam obstructed by a transparent particle. *Opt. Commun.* **2013**, *286*, 135–139. [CrossRef]
11. Vaity, P.; Singh, R.P. Self-healing property of optical ring lattice. *Opt. Lett.* **2011**, *36*, 2994–2996. [CrossRef]
12. Ring, J.D.; Lindberg, J.; Mourka, A.; Mazilu, M.; Dholakia, K.; Dennis, M.R. Auto-focusing and self-healing of Pearcey beams. *Opt. Express* **2012**, *20*, 18955–18966. [CrossRef] [PubMed]
13. Cao, R.; Hua, Y.; Min, C.; Zhu, S.; Yuan, X.C. Self-healing optical pillar array. *Opt. Lett.* **2012**, *37*, 3540–3542. [CrossRef] [PubMed]
14. Wu, G.; Wang, F.; Cai, Y. Generation and self-healing of a radially polarized Bessel-Gauss beam. *Phys. Rev. A* **2014**, *89*, 043807. [CrossRef]
15. Garces-Chavez, V.; McGloin, D.; Melville, H.; Sibbett, W.; Dholakia, K. Simultaneous micromanipulation in several planes using a self-reconstructing light beam. *Nature* **2002**, *419*, 145–147. [CrossRef]
16. Fahrbach, F.O.; Simon, P.; Rohrbach, A. Microscopy with self-reconstructing beam. *Nat. Photonics* **2010**, *4*, 780–786. [CrossRef]
17. Ricklin, J.C.; Davidson, F.M. Atmospheric optical communication with a Gaussian Schell beam. *J. Opt. Soc. Am. A* **2003**, *20*, 856–866. [CrossRef] [PubMed]
18. Zeng, Z.S.; Zhao, D.M. Partially Coherent Dual Nonparaxial Accelerating Beams. *Ann. Phys.* **2021**, *533*, 2000438. [CrossRef]
19. Ata, Y.; Yao, J.R.; Korotkova, O. BER variation of an optical wireless communication system in underwater turbulent medium with any temperature and salinity concentration. *Opt. Commun.* **2021**, *485*, 126751. [CrossRef]
20. Wang, F.; Chen, Y.; Liu, X.; Cai, Y.; Ponomarenko, S.A. Self-reconstruction of partially coherent light beams scattered by opaque obstacles. *Opt. Express* **2016**, *24*, 23735–23746. [CrossRef]
21. Zhou, Y.P.; Wu, G.F.; Cai, Y.J.; Wang, F.; Hoenders, B.J. Application of self-healing property of partially coherent beams to ghost imaging. *Appl. Phys. Lett.* **2020**, *117*, 171104. [CrossRef]
22. Wu, G.; Tao, C. Analytical study of the self-reconstruction of a partially coherent Gaussian Schell-model beam. *Opt. Commun.* **2018**, *424*, 86–90. [CrossRef]
23. Xu, Z.; Liu, X.; Chen, Y.; Wang, F.; Liu, L.; Monfared, Y.E.; Ponomarenko, S.A.; Cai, Y.; Liang, C. Self-healing properties of Hermite-Gaussian correlated Schell-model beams. *Opt. Express* **2020**, *28*, 2828–2837. [CrossRef]
24. Peng, X.; Wang, H.; Liu, L.; Wang, F.; Popov, S.; Cai, Y. Self-reconstruction of twisted Laguerre-Gaussian Schell-model beams partially blocked by an opaque obstacle. *Opt. Express* **2020**, *28*, 31510–31523. [CrossRef]
25. Liu, X.; Peng, X.; Liu, L.; Wu, G.; Zhao, C.; Wang, F.; Cai, Y. Self-reconstruction of the degree of coherence of a partially coherent vortex beam obstructed by an opaque obstacle. *Appl. Phys. Lett.* **2017**, *110*, 181104. [CrossRef]
26. Zhou, Y.; Cui, Z.; Han, Y. Polarization and coherence properties in self-healing propagation of a partially coherent radially polarized twisted beam. *Opt. Express* **2022**, *30*, 23448–23462. [CrossRef]
27. De Santis, P.; Gori, F.; Guattari, G.; Palma, C. A space-time modulated field with specular coherence function. *Opt. Commun.* **1987**, *64*, 9–14. [CrossRef]
28. Gori, F.; Guattari, G.; Palma, C.; Padovani, C. Specular cross-spectral density functions. *Opt. Commun.* **1988**, *68*, 239–243. [CrossRef]
29. Partanen, H.; Sharmin, N.; Tervo, J.; Turunen, J. Specular and antispecular light beams. *Opt. Express* **2015**, *23*, 28718–28727. [CrossRef]
30. Zhou, Z.; Guo, M.; Zhao, D. Influence of atmospheric turbulence on the properties of specular and antispecular beams. *Appl. Opt.* **2016**, *55*, 6757. [CrossRef] [PubMed]
31. Guo, M.; Zhao, D. Changes in radiation forces acting on a Rayleigh dielectric sphere by use of a wavefront-folding interferometer. *Opt. Express* **2016**, *24*, 6115. [CrossRef]
32. Das, D.; Halder, A.; Partanen, H.; Koivurpva, M.; Turunen, J. Propagation of Bessel-correlated specular and antispecular beams. *Opt. Express* **2022**, *30*, 5709–5721. [CrossRef] [PubMed]
33. Tang, M.M.; Feng, X.X.; Liu, S.Y.; Li, H.H.; Li, X.Z. Transformation of asymmetric Schell-model beams with a wavefront-folding interferometer. *J. Opt.* **2021**, *23*, 045605. [CrossRef]
34. Guo, M.; Zhao, D. Polarization properties of stochastic electromagnetic beams modulated by a wavefront-folding interferometer. *Opt. Express* **2018**, *26*, 8581. [CrossRef]
35. Tang, M.M.; Dong, S.J.; Yang, Y.Z.; Zhou, Y.J.; Guo, M.W.; Li, X.Z. Specular transformation of electromagnetic partially coherent beams with a wave-folding interferometer. *J. Opt.* **2024**, *26*, 065601. [CrossRef]
36. Wu, G. Propagation properties of a radially polarized partially coherent twisted beam in free space. *J. Opt. Soc. Am. A* **2016**, *33*, 345–350. [CrossRef] [PubMed]
37. Liu, L.; Peng, X.; Chen, Y.; Guo, L.; Cai, Y. Statistical properties of a radially polarized twisted Gaussian Schell-model beam in a uniaxial crystal. *J. Mod. Opt.* **2017**, *64*, 698–708. [CrossRef]
38. Fu, W.; Cao, P. Second-order statistics of a radially polarized partially coherent twisted beam in a uniaxial crystal. *J. Opt. Soc. Am. A* **2017**, *34*, 1703–1710. [CrossRef] [PubMed]

39. Peng, X.; Liu, L.; Cai, Y.; Baykal, Y. Statistical properties of a radially polarized twisted Gaussian Schell-model beam in an underwater turbulent medium. *J. Opt. Soc. Am. A* **2017**, *34*, 133–139. [CrossRef] [PubMed]
40. Peng, X.; Liu, L.; Yu, J.; Liu, X.; Cai, Y.; Baykal, Y.; Li, W. Propagation of a radially polarized twisted Gaussian Schell-model beam in turbulent atmosphere. *J. Opt.* **2016**, *18*, 125601. [CrossRef]
41. Liu, Z.; Wang, X.; Huang, K. Scattering of polychromatic partially coherent radially polarized twisted beams upon a deterministic medium. *J. Opt. Soc. Am. B* **2020**, *37*, 2989–2995. [CrossRef]
42. Wolf, E. *Introduction to the Theory of Coherence and Polarization of Light*; Cambridge University: Cambridge, UK, 2007.
43. Halder, A.; Partanen, H.; Leinonen, A.; Koivurova, M.; Hakala, T.; Setälä, T.; Turunen, J.; Friberg, A. Mirror-based scanning wavefront-folding interferometer for coherence measurements. *Opt. Lett.* **2020**, *45*, 4260–4263. [CrossRef] [PubMed]
44. Korotkova, O.; Wolf, E. Generalized Stokes parameters of random electromagnetic beams. *Opt. Lett.* **2005**, *30*, 198–200. [CrossRef] [PubMed]

Disclaimer/Publisher's Note: The statements, opinions and data contained in all publications are solely those of the individual author(s) and contributor(s) and not of MDPI and/or the editor(s). MDPI and/or the editor(s) disclaim responsibility for any injury to people or property resulting from any ideas, methods, instructions or products referred to in the content.